nature astronomy

Article

https://doi.org/10.1038/s41550-023-02099-2

An intense narrow equatorial jet in Jupiter's lower stratosphere observed by JWST

Received: 25 April 2023

Accepted: 11 September 2023

Published online: 19 October 2023

Check for updates

Ricardo Hueso[1] ✉, Agustín Sánchez-Lavega[1], Thierry Fouchet[2], Imke de Pater[3,4], Arrate Antuñano[1], Leigh N. Fletcher[5], Michael H. Wong[6,7], Pablo Rodríguez-Ovalle[2], Lawrence A. Sromovsky[8], Patrick M. Fry[8], Glenn S. Orton[9], Sandrine Guerlet[2,10], Patrick G. J. Irwin[11], Emmanuel Lellouch[2], Jake Harkett[5], Katherine de Kleer[12], Henrik Melin[5], Vincent Hue[13], Amy A. Simon[14], Statia Luszcz-Cook[15,16] & Kunio M. Sayanagi[17]

The atmosphere of Jupiter has east–west zonal jets that alternate as a function of latitude as tracked by cloud motions at tropospheric levels. Above and below the cold tropopause at ~100 mbar, the equatorial atmosphere is covered by hazes at levels where thermal infrared observations used to characterize the dynamics of the stratosphere lose part of their sensitivity. James Webb Space Telescope observations of Jupiter in July 2022 show these hazes in higher detail than ever before and reveal the presence of an intense (140 m s^{-1}) equatorial jet at 100–200 mbar (70 m s^{-1} faster than the zonal winds at the cloud level) that is confined to ±3° of the equator and is located below stratospheric thermal oscillations that extend at least from 0.1 to 40 mbar and repeat in multiyear cycles. This suggests that the new jet is a deep part of Jupiter's Equatorial Stratospheric Oscillation and may therefore vary in strength over time.

Jupiter and Saturn atmospheres have zonal jets with broad prograde winds in their equatorial regions[1,2]. The winds are best observed at cloud-top levels but extend 3,000 km deeper in Jupiter[3,4] and 8,000 km in Saturn[5,6]. Above the cloud level, wind speeds decay with increasing altitude to nearly zero values at 20 mbar in most of Jupiter's mid-latitudes[7–9]. However, this pattern of vertical decay is spectacularly broken in Saturn's equator, where an intense (400 m s^{-1}) and narrow (5° width) jet is observed tracking the motions of high-altitude hazes at the 50–60 mbar level[10,11].

In the equatorial regions of both planets, temperature retrievals through infrared spectroscopy, in combination with the thermal wind relationship[12,13], reveal the presence of intense stratospheric eastward and westward winds alternating in direction as a function of altitude in the 0.1–40.0 mbar region[8,14,15]. The perturbations to the equatorial stratospheric temperatures and inferred thermal winds vary periodically on multiyear timescales[15–18], sharing characteristics with similar phenomena on Earth, such as the quasi-biennial oscillation (QBO) and semi-annual oscillation (SAO)[12,19]. Like their terrestrial counterparts, Jupiter and Saturn's equatorial stratospheric oscillations form a vertical pattern of temperature and wind perturbations that gradually descends over time[20–23]. Jupiter's equatorial stratospheric oscillation

[1]Escuela de Ingeniería de Bilbao, Universidad del País Vasco, UPV/EHU, Bilbao, Spain. [2]LESIA, Observatoire de Paris, Université PSL, CNRS, Sorbonne Université, Université de Paris, Meudon, France. [3]Department of Astronomy, University of California, Berkeley, CA, USA. [4]Department of Earth & Planetary Science, University of California, Berkeley, CA, USA. [5]School of Physics and Astronomy, University of Leicester, Leicester, UK. [6]Center for Integrative Planetary Science, University of California, Berkeley, CA, USA. [7]Carl Sagan Center for Research, SETI Institute, Mountain View, CA, USA. [8]Space Science and Engineering Center, University of Wisconsin, Madison, WI, USA. [9]Jet Propulsion Laboratory, California Institute of Technology, Pasadena, CA, USA. [10]Laboratoire de Météorologie Dynamique (LMD/IPSL), Sorbonne Université, ENS, PSL Research University, Ecole Polytechnique, Institut Polytechnique de Paris, CNRS, Paris, France. [11]Department of Physics, University of Oxford, Oxford, UK. [12]California Institute of Technology, Pasadena, CA, USA. [13]Aix-Marseille Université, CNRS, CNES, Institut Origines, LAM, Marseille, France. [14]Solar System Exploration Division, NASA Goddard Space Flight Center, Greenbelt, MD, USA. [15]Department of Astronomy, Columbia University, New York City, NY, USA. [16]Astrophysics Department, American Museum of Natural History, New York, NY, USA. [17]NASA Langley Research Center, Hampton, VA, USA. ✉e-mail: ricardo.hueso@ehu.eus

https://doi.org/10.1038/s41550-023-02099-2

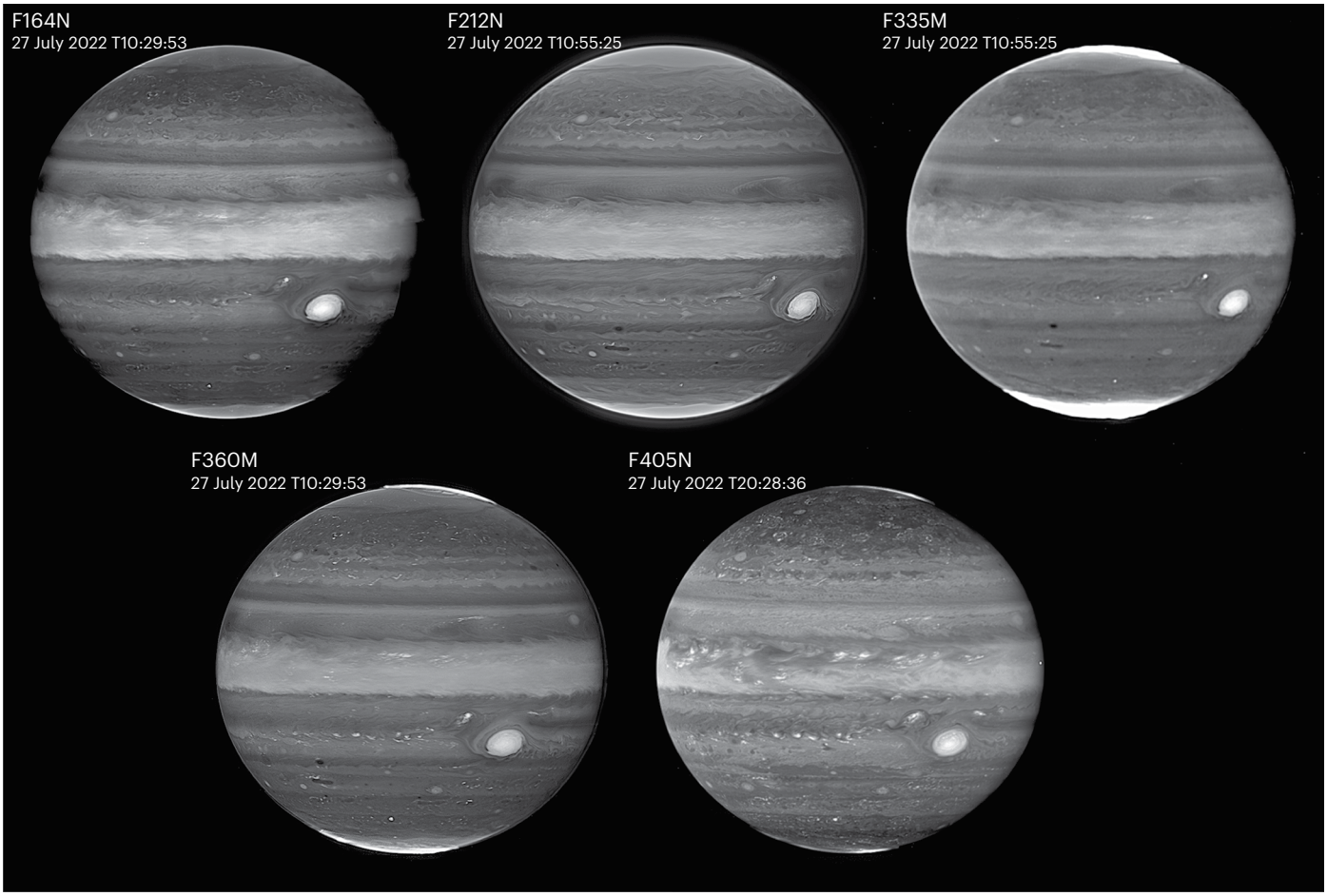

Fig. 1 | NIRCam images of Jupiter. Images are shown after combining individual frames in the same filter which differed in their acquisition time by a few minutes. These frames were first corrected for the rotation of the planet. A high-pass filter was applied to enhance the contrast. A linear-stretch version of this figure without high-pass processing is available as Supplementary Fig. 1. Images in the F164N filter were obtained in subarrays and mosaicked into a single image compensating for the rotational effects of the 16 individual frames that were used. Images in the F164N and F212N filters have a pixel scale of 0.03087 arcsec pixel^{-1} (roughly 99 km pixel^{-1} on Jupiter's disc). Images in the F335M, F360M and F405N filters have a pixel scale of 0.06303 arcsec pixel^{-1} (203 km pixel^{-1}).

(JESO) has a variable period of 3.9 to 5.7 years with the variability linked to the occasional development of large-scale convective perturbations[20,24]. Saturn's equatorial stratospheric temperatures oscillate quasi-periodically in a 15-year cycle (that is, half a Saturn year)[18], but this period can also be disrupted by large convective storms developing at other latitudes[25]. Variations of temperatures in Jupiter's upper troposphere have been observed down to 300 mbar with a periodicity at the equator of 8 years and an anticorrelated relation with the JESO at near-equatorial latitudes[26]. The complex phenomenology at the equatorial regions of Jupiter and Saturn points to connections between the stratospheric and tropospheric dynamics that are not well understood.

Elevated hazes cover Jupiter's equatorial region around and above the 200 mbar level[27–29]. These hazes are variable in opacity and albedo, and their brightness in the methane absorption band at 890 nm can vary up to 30% over different years[30,31]. The equatorial hazes are situated well above the tropospheric clouds, where winds are well-characterized by trackable cloud features, and well below the stratospheric region, where temperature retrievals from thermal infrared observations allow deducing winds through the thermal wind analysis. However, the hazes appear mostly featureless, preventing high-quality measurements of winds at their altitude[32,33]. Ultraviolet (UV) images acquired by the Cassini spacecraft, representative of the 500 mbar level, showed that right at the equator about 4–5 km above the cloud tops at around 600 mbar, zonal winds increase slightly (10 m s^{-1}) with increasing altitude[33], but those measurements had large uncertainties due to the low contrast in UV images.

Observations

We observed Jupiter's atmosphere on 27 July 2022 using the Near Infrared Camera (NIRCam) instrument[34] on the James Webb Space Telescope (JWST) as part of the Jupiter System Early Release Science Program no. 1373 (ref. 35). Because Jupiter is a bright target for JWST, we selected filters centred in strong atmospheric methane absorption bands (F164N, F335M, F360M and F405N) and in the strong H_2–H_2 and H_2–He collision-induced absorption band at 2.12 μm (F212N), and obtained full-disk images of the planet. We repeated our observations after one planetary rotation (about 10 h) to observe the same hemisphere twice and examine temporal changes and dynamics, with the exception of filters F360M and F405N, which were only used once. Figure 1 shows NIRCam images processed with a high-pass spatial filter to emphasize fine-scale details (Supplementary Table 1 gives details about the images and Supplementary Fig. 1 shows these images without high-pass filtering). The Methods provides details about the image acquisition and processing techniques.

Ground-based and Hubble Space Telescope (HST) observations of Jupiter at these wavelengths generally result in images with very low contrast in which most fine-scale atmospheric details cannot be resolved[36]. Our JWST observations clearly resolve fine-scale details all

https://doi.org/10.1038/s41550-023-02099-2

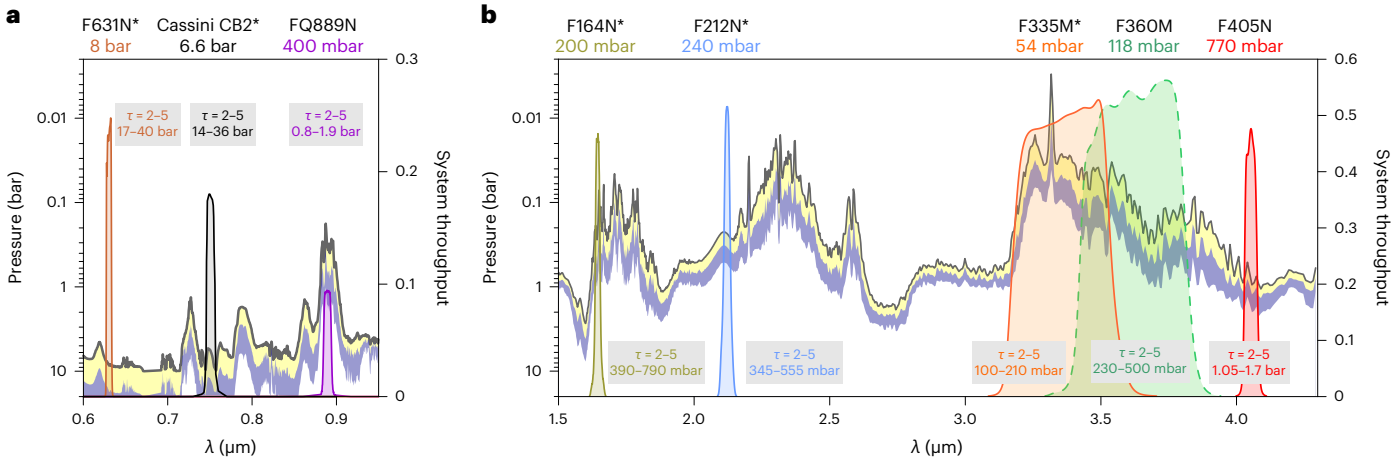

Fig. 2 | Pressure at which two-way vertical optical depth τ reaches 1 (black line) for a model atmosphere with no aerosols. The model atmosphere with no aerosols is based on ref. 37. The yellow shaded region shows the two-way vertical optical depths from 1 to 2. The grey-blue shaded area shows the two-way vertical optical depths from 2 to 5. The curves are compared with system throughputs for different filters. Filters marked with * are those for which winds have been obtained in the past (F631N, and the CB2 filter on the Cassini/ISS), or in this work (F164N, F212N, F335M). For each filter, the mean pressure level sensed ($\tau = 1$) is given at the top, and the range of levels that can be sensed with optical depths of 2–5 is given next to each filter in the figure. λ is the light wavelength measured in μm. **a**, Selection of filters in which atmospheric dynamics have been studied in the past (F631N filter in HST/WFC3 instrument, the CB2 filter on Cassini/ISS and the FQ889N filter in HST/WFC3 centred at a strong methane absorption band. **b**, Filters used in our JWST/NIRCam observations.

over the planet at all wavelengths. Thus, the image quality provided by JWST enables new capabilities to study Jupiter's atmospheric dynamics at the altitudes sampled.

The JWST filters in which we observed Jupiter are sensitive to a mixture of tropospheric and stratospheric hazes (Fig. 1; filters F335M, F360M and F405N are also sensitive to H_3^+ emissions from polar auroras which will be discussed in a separate paper). Figure 2 shows the sensitivity of JWST/NIRCam filters to different altitudes for a simplified model atmosphere that assumes no aerosols and considers only gaseous absorptions and Rayleigh scattering[37]. We show the two-way penetration depth of solar radiation in Jupiter's atmosphere considering optical depths from $\tau = 1$ to $\tau = 5$. Sensing levels by these filters will depend on the structure of clouds and hazes and will be different in different locations of the planet. For each filter, regions with clouds or hazes located at altitudes with low optical depths will appear bright (an example is the Great Red Spot (GRS)) (Fig. 1). In filters with strong atmospheric absorption bands, regions with tropospheric clouds without substantial haze above them will appear dark (like the area around the GRS and most locations over the planet in Fig. 1).

In the filters F164N, F212N, F335M and F360M, unenhanced images in Supplementary Fig. 1 show large brightness differences between the equatorial zone (EZ), the GRS, the polar areas and the rest of the planet. In the F405N filter, which is not affected by notable absorption from gases, the contributions of low optical depth small particle hazes are greatly diminished, and the tropospheric levels where the clouds become optically thick are sensed. Comparing these multiwavelength images, we see that outside of the EZ, the GRS and the polar areas, all JWST images show the same features sensing the main cloud deck in the troposphere (500–700 mbar).

The EZ in the F164N, F212N, F335M and F360M images is roughly 5, 9, 4 and 2 times brighter respectively than the mid-latitudes. The high brightness difference of the EZ from the rest of the atmosphere in the F212N and F164N filters suggests that in both filters we are observing the low-opacity hazes at elevated altitudes close to $\tau = 1$, while in filters sensitive both to the lower stratosphere and the upper troposphere (F335M and F360M), the contrast between elevated and deep features is reduced. At the EZ, these two filters have contributions from haze layers above those sensed with the F212N and F164N filters mixed with deeper features in the troposphere. The approximate levels sensed in the EZ in our observations are summarized in Table 1, where they are compared with levels sensed in the past to investigate cloud motions.

JWST/NIRCam images show an amount of detail in the equatorial hazes (Fig. 3) that largely surpasses those of any previous images of Jupiter at these wavelengths. The 2.12 μm images show crisp features (highlighted in Fig. 3) that have bright counterparts in all other JWST filters and seem to be associated with bright and compact clouds in the lower troposphere as observed in the F405N image. These features may represent either convective activity, or a vertical connection between tropospheric clouds and features located at least one scale height above the main cloud deck.

Supplementary Fig. 2 shows HST images and maps of the equatorial region obtained on 28 July 2022 two Jupiter rotations after the JWST images shown in Fig. 3. Some of the bright cloud systems in the F405N images show convective activity in these HST images of the cloud level. Time-resolved ground-based observations of Jupiter obtained through July 2022 and available at the PVOL database (http://pvol2.ehu.eus) and ALPO Japan website (https://alpo-j.sakura.ne.jp/indexE.htm) confirm that the planet's atmosphere was relatively quiescent, with no major convective outbreaks.

Wind results

We tracked the motions of atmospheric features observed in the F164N, F212N and F335M images by comparing map-projected images of the planet separated in time by one planetary rotation. We used image correlation software designed for cloud-tracking wind analysis[38–40] and excluded from the analysis regions covered by large atmospheric systems like the GRS (Methods). Figure 4 shows our wind results.

Outside of the EZ, our new JWST-based zonal wind profiles are very similar to prior measurements of Jupiter's zonal winds at the cloud tops[39,41,42] (Fig. 4a). This is because out of the EZ, the cloud systems tracked in NIRCam images are the same as those visible in HST and ground-based images (Supplementary Fig. 2), that is, the absence of elevated aerosols across most of the planet allows these filters to sense the lower troposphere. The quality of the wind retrievals at high latitudes (Fig. 4a) is progressively deteriorated by the increasing opacity of elevated subpolar hazes that obstruct views of the tropospheric clouds. Throughout the EZ, at latitudes ±10° (all latitudes in this paper are planetographic), the derived zonal winds represent the motions

https://doi.org/10.1038/s41550-023-02099-2

Table 1 | Approximate sensing levels in the EZ when taking into account clouds and hazes

Source	Filter	λ_{eff} (μm)	Pressure level (mbar)	Primary sensed aerosol layers EZ
HST/WFC3 and Cassini/ISS	UV1	0.264	315–500[a]	Equatorial haze
	F631N	0.630	500–600[b]	Tropospheric clouds
	CB2	0.750	500–600[b]	Tropospheric clouds
	FQ889N	0.889	200–400[b]	Equatorial haze
JWST/NIRCam	F212N	2.120	~240	Equatorial haze
	F164N	1.644	~200	Equatorial haze
	F335M	3.365	50–500	Equatorial haze+ tropospheric clouds
	F360M	3.621	100–500	Equatorial haze+tropospheric clouds
	F405N	4.055	500–600	Tropospheric clouds

λ_{eff} is the pivot wavelength for each filter[51]. CB2, Continuum Band 2; ISS, Imaging Science Subsystem; WFC3, Wide Field Camera 3. [a] From ref. 33. [b] From ref. 29.

of the upper hazes, which show a very different behaviour from the motions at the main cloud layer. A distinct central narrow and intense jet is observed at the three wavelengths where JWST obtained data on two consecutive rotations of the planet (F164N, F212N and F335M). Outside of the central narrow jet, but still inside the EZ, JWST images show a decrease in the zonal winds at higher altitudes with respect to the winds at the cloud tops. This decrease in the wind intensity with altitude has some minor differences between the northern edge of the EZ and the southern edge. The latitudinal asymmetry in the winds may relate to different haze opacities north and south of the equator. JWST observed higher haze opacity in the southern branch of the EZ, as illustrated in Fig. 3, but we note that previous studies have shown that the latitudinal asymmetry in haze distribution is variable on timescales of a few years[31].

In the F212N observations, zonal winds in the EZ from the cloud correlation analysis have lower dispersions than in the F164N and F335M filters. In the F212N images, details are better contrasted and individual cloud features can be visually identified and tracked after a planetary rotation (Supplementary Fig. 3 displays a selection of those features, blue dots in Fig. 4b depict the velocity of the full sample of visually identified cloud-tracking details). However, many of the crisp features highlighted in Fig. 3 have no counterparts one rotation later, or appear very distorted on the next planetary rotation, which is consistent with the presence of strong wind shears.

The wind measurements in the EZ obtained in the F164N and F335M filters have larger dispersions than those from the F212N images (Fig. 4c). This is caused by a combination of different factors. First, the wind measurements in F164N images were obtained in subarrays with narrower views of the EZ. This results in smaller sizes of the regions where cloud correlation can be calculated. Secondly, the F335M images have half the spatial resolution of the F164N and F212N images and are also subject to higher noise levels. Finally, the F164N and F335M images are both sensitive to a wider vertical column of the atmosphere than the F212N images. Thus, we cannot discount the possibility that part of the wind dispersion in these two filters is created by tracking features at different altitudes through the vertical range of levels sensed by these filters and affected by vertical wind shear.

Our measurements show that the zonal winds at the equator increase in height from the cloud tops at around 600 mbar in the EZ[29], where the zonal wind profile has a local minimum of 70 m s^{-1}, to the tropopause at 100–200 mbar, where the zonal wind profile has a local maximum of 140 m s^{-1} in the F335M filter. The different wind values at the equator obtained in F212N (105 ± 16 m s^{-1}), F164N (115 ± 35 m s^{-1}) and F335M (140 ± 20 m s^{-1}) images suggest the presence of a strong vertical wind shear within the haze levels, with the most intense winds observed in the F335M images most likely sensing the highest levels (Supplementary Fig. 4). Furthermore, UV-measurements of zonal winds during the Cassini flyby in 2000 found zonal winds of 82 ± 11 m s^{-1} at 500 mbar (ref. 33), supporting the hypothesis that most of the vertical wind shear in this central equatorial jet is concentrated through the hazes. Right at the equator, we estimate mean vertical wind shears from the cloud tops to the hazes of 40–70 m s^{-1} per scale height (~20 km), with more uncertain wind shears of 10–110 m s^{-1} per scale height within the hazes (Supplementary Fig. 4). Outside the central jet at ±3°, but still in the EZ (±10°), the winds decrease in height, with the strongest shear at ±7°, where the zonal winds decrease from the cloud tops to the equatorial hazes by 45–60 m s^{-1}. This results in a mean vertical wind shear of −25 to −60 m s^{-1} per scale height, which is comparable but opposite in sign to the vertical shear at the equator.

Discussion

The new equatorial jet near Jupiter's tropopause makes Jupiter's and Saturn's equatorial circulations remarkably similar (Fig. 5). Both planets harbour a doubly peaked equatorial jet at the main cloud level observable in visible wavelengths. Our new JWST observations show that Jupiter has in addition a sharply peaked jet right at the equator (±3°) in the hazes above the main cloud deck. The wind speed in the narrow jet increases with altitude up to the tropopause, while it decays with altitude outside of the central jet. A similar wind structure was found previously on Saturn's equator, except that the central jet in Jupiter increases in altitude much more strongly than on Saturn. Jupiter's central equatorial jet is located in a region of the EZ that appears brighter than the rest of the EZ at 889 nm and at F335M (Fig. 5). On Jupiter and Saturn, the zonal wind profiles at cloud level have two local maxima near ±10° in Jupiter and ±15° in Saturn that move poleward with increasing height. Besides these similarities, there are also differences between the equatorial winds in both planets. Jupiter's EZ is narrower in latitude than Saturn's EZ and the observed meteorology at cloud level is very different[11,43]. In addition, in Jupiter the increase in wind intensity with altitude at the equator (40–70 m s^{-1} per scale height; see also Supplementary Fig. 4) is notably larger than the one in Saturn (8 m s^{-1} per scale height in the Cassini epoch)[11]. However, these vertical shears could be variable in time if the jets at the upper hazes follow temporal variations similar to the oscillations in stratospheric temperatures and winds.

The equatorial stratospheric thermal oscillations and associated winds in Jupiter and Saturn also share similarities and differences[8,14–18,20–25]. Among the latter, the different periods of JESO (3.9–5.7 years[20,24]) and Saturn's SAO (15 years[18]) argue for different dynamical origins. The half Saturn year cycle of Saturn's SAO suggests a seasonal effect[43], while the time periods and phenomenology of the JESO cannot be related with seasons. JESO is reminiscent of the Earth's QBO[19,44], a downward propagating easterly and westerly wind pattern that affects the 5–50 mbar portion of the Earth's atmosphere. Although the QBO phenomenology on Earth is not fully understood, gravity waves created by convection in the lower troposphere are known to play a major role releasing energy and momentum in the Earth's stratosphere[19,43]. Similar mechanisms, such as the forcing created by gravity waves originating from convection in the troposphere, have been proposed for Jupiter's thermal oscillations[16,45]. Our JWST observation in F405N in Figs. 1 and 3, and the context views of the lower atmosphere in Supplementary Fig. 2, show bright cloud systems of possible convective nature with small-scale bright systems observable in the upper hazes.

Our JWST observations provide new insights into the troposphere-stratosphere interactions in Jupiter, and can inform us about the depth of penetration into the troposphere of the equatorial oscillation. On Earth, the QBO does not penetrate below the tropopause, but on Jupiter, the unexpected presence of this intense and elevated equatorial jet, which is not reproduced in existing simulations, suggests

https://doi.org/10.1038/s41550-023-02099-2

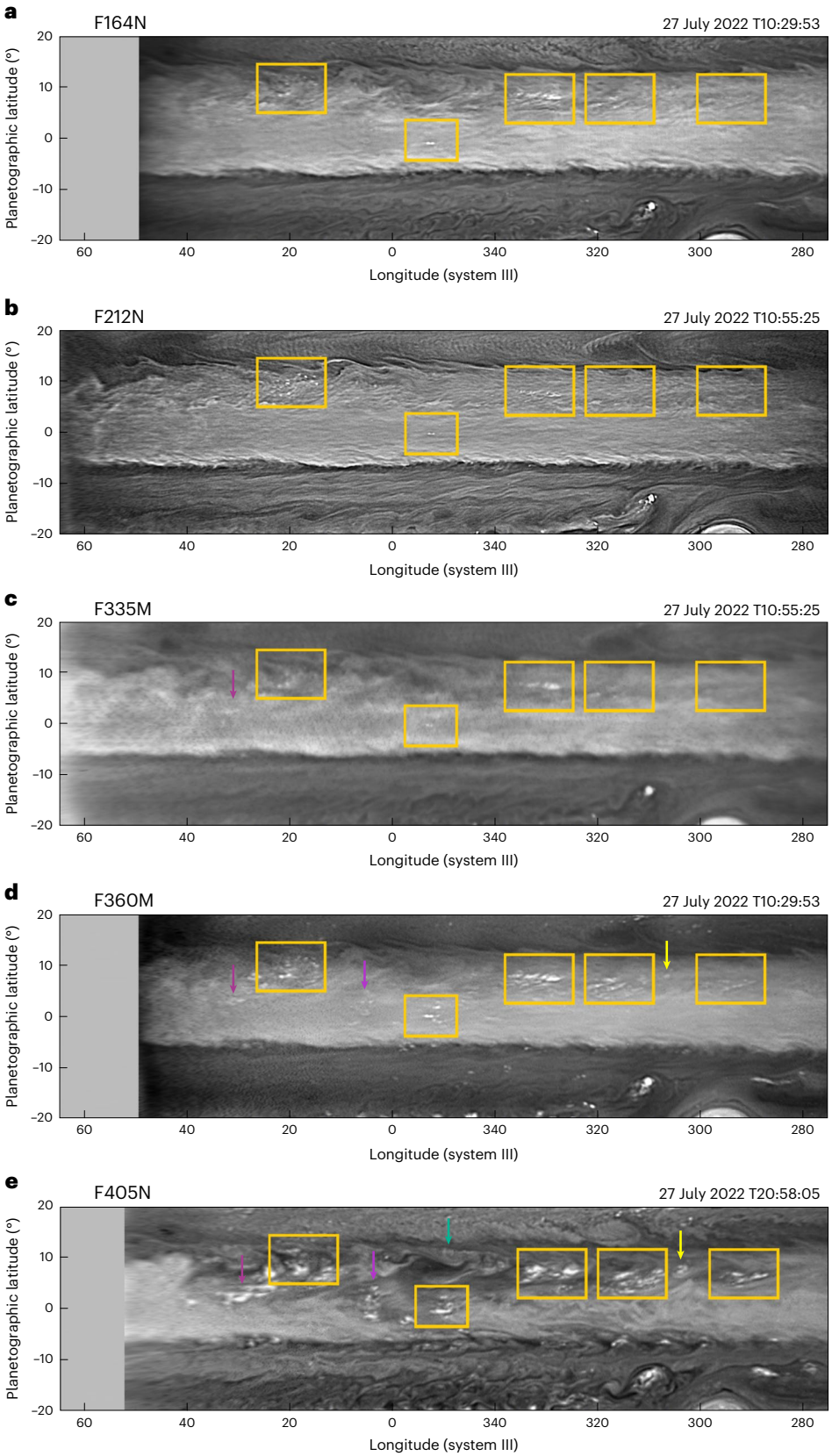

Fig. 3 | Multiwavelength maps of the equatorial region. a–**e**, Images in **a**–**d** were obtained close in time and the image in **e** was obtained after one planetary rotation (Supplementary Table 1), using filters F164N (**a**), F212N (**b**), F335M (**c**), F360M (**d**) and F405N (**e**). All images have been processed with a high-pass spatial filter to show the smallest-scale details. Boxes show bright features in the lower troposphere observed in the F405N image with counterparts in the upper hazes. Purple arrows indicate bright details observable in the F405N image with counterparts only in some of the images of the upper hazes. Yellow arrows show a convective storm also active in HST observations taken one rotation later (Supplementary Fig. 2). The green arrow in **e** shows the location of a deep cloud system that developed into a convective storm one Jupiter rotation later as observed in HST images.

https://doi.org/10.1038/s41550-023-02099-2

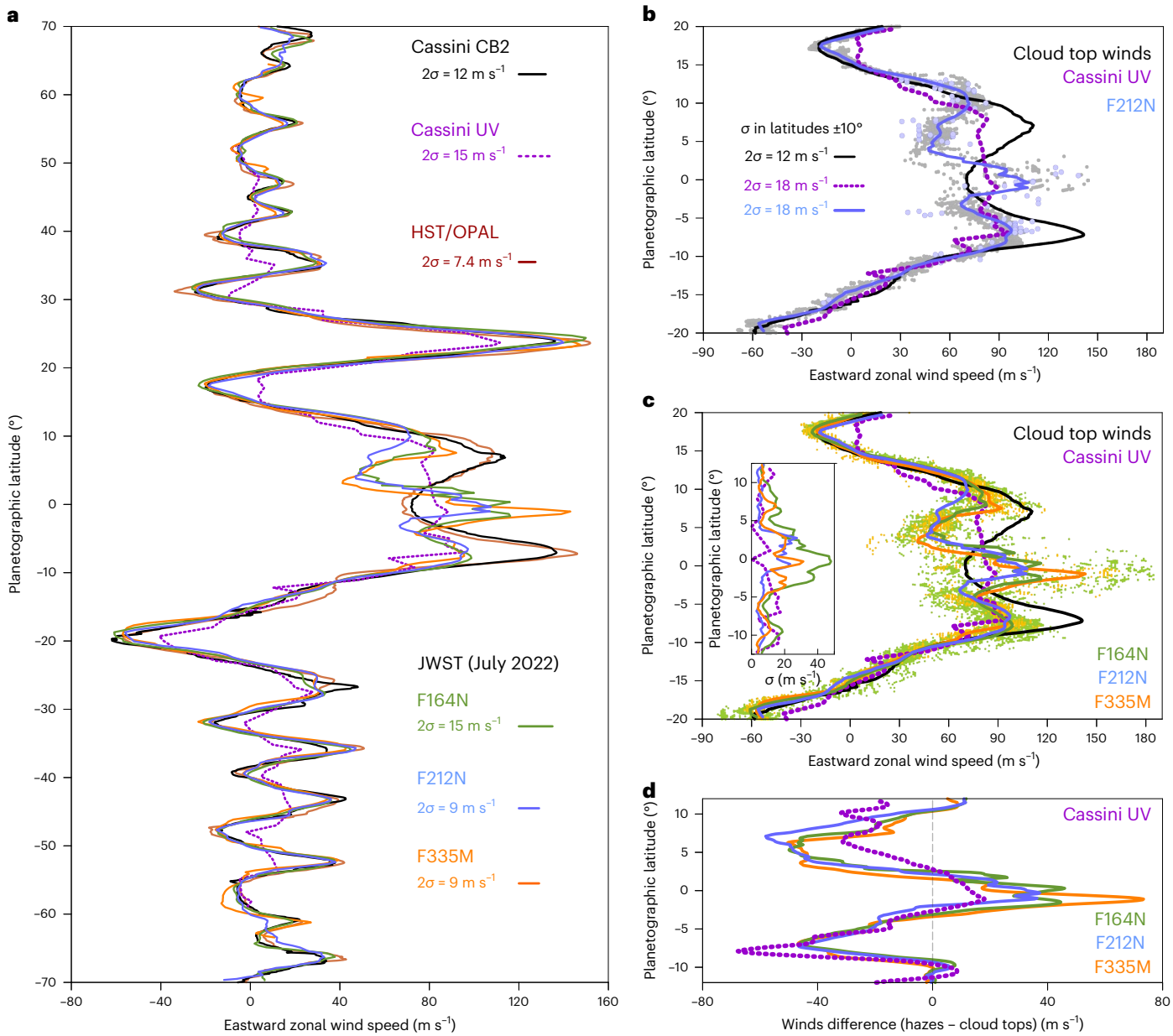

Fig. 4 | Jupiter's zonal wind profile. Zonal winds from JWST images are compared with zonal winds measured on Cassini UV images[33], on continuum filters at cloud level[41], and on HST images acquired in 2019 and analysed following the procedure in ref. 39. **a**, Mean zonal winds. **b**, Zonal winds at the equator. A black line shows the average of Cassini data from the year 2000 and HST data from 2019. The blue line is the F212N zonal mean winds. Grey symbols correspond to measurements of F212N images using the cloud correlation software. Blue circles correspond to cloud features visually tracked in F212N images. Mean error bars from twice the standard deviation (2σ) are shown as segments for each wind profile in **a** and for the ±10° latitudes in **b**. **c**, Zonal winds in the F164N, F212N and F335M filters in the equator compared with cloud-top winds and winds measured on Cassini UV images. Dots are individual measurements from the correlation software and lines are mean zonal winds. The inset shows the standard deviation of zonal winds in each filter considering latitudinal bins of width 0.3°, except for the Cassini UV data, which used latitudinal bins of 1°. **d**, Wind difference between the different filters sampling the hazes and the clouds tops. A dotted grey line shows the zero value.

the stratospheric equatorial oscillations penetrate into the upper troposphere in an unanticipated way. The stratospheric oscillations are variable in both Jupiter and Saturn, and the time variability of the jet at the base of the stratosphere remains uncertain given that we have only observed Jupiter's lower stratospheric jet during a single epoch. Thermal maps of Jupiter acquired in mid-2019 (ref. 20), extrapolated in time to 2022 using the descent rate of the JESO observed during its last cycle, suggest that the ~40 mbar level had a warm anomaly during our JWST observations. This would be consistent with winds decreasing at greater depths as observed in our JWST images. This extrapolation in time also suggests a change in the sign of the thermal perturbation at 40 mbar in 2023–2024, allowing an examination of the time-variable component of the equatorial jet.

A combined view of Jupiter's equatorial dynamics from the cloud tops to the upper stratosphere can be obtained by combining observations in the visible (500–700 mbar), near-infrared (100–200 mbar), thermal infrared (1–40 mbar), and Doppler winds from millimeter data (~4 mbar), where intense equatorial zonal winds have been observed[46,47]. At 500–700 mbar, wind measurements at visible wavelengths hint at variability (<10 m s^{-1}) with possible periods of 5–7 years[48], while at

https://doi.org/10.1038/s41550-023-02099-2

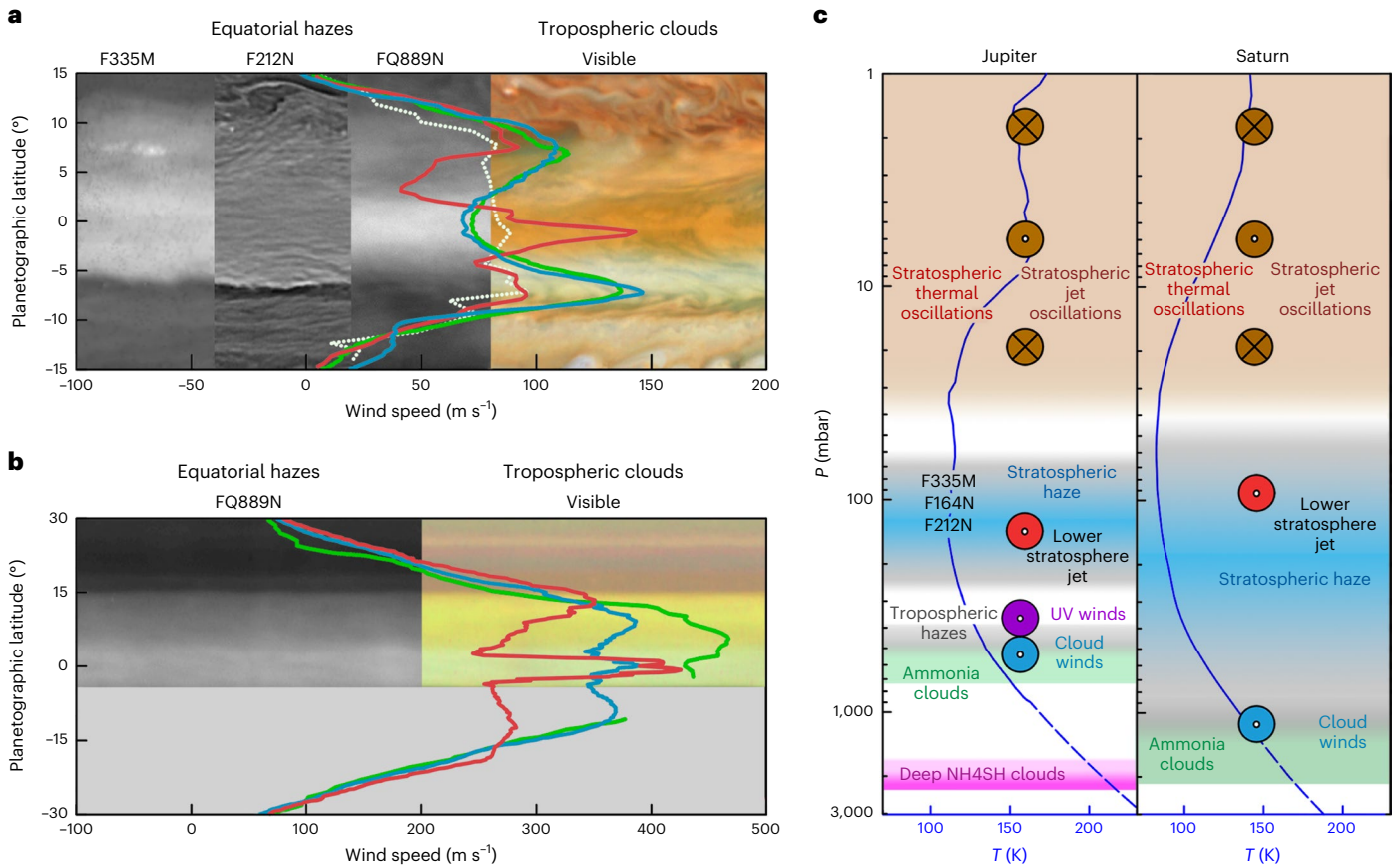

Fig. 5 | Sketch of Jupiter and Saturn equatorial dynamics. a, Jupiter's EZ and equatorial winds from Cassini (green line cloud tops, white dots UV), HST (blue) and JWST F335M wind profile (red). Background images show the morphology of the EZ in different wavelengths. **b**, Saturn's EZ and equatorial winds from Voyager (green line), Cassini deeply penetrating filters (blue) and Cassini filters sampling the 889-nm methane absorption band (red). Background images show Saturn's EZ in different wavelengths observed in 2022 by HST, with the grey region covered by the rings. **c**, Sketch of the different cloud layers and levels where zonal winds are observed (circles). Both the cloud-top winds and the winds at the hazes are eastward, but winds in the upper stratosphere alternate eastward or westward depending on the altitude level and the phase of the thermal oscillation. P, atmospheric pressure measured in millibars; T, atmospheric temperature measured in Kelvin.

stratospheric levels the periodicity in the temperature oscillations and winds is 4–6 years[20,24]. In the near-infrared windows in which the upper hazes are observable at intermediate levels between the cloud tops and the stratosphere, only new observations by JWST can determine the atmospheric circulation and its expected variability. The equatorial dynamics of Jupiter and Saturn are complex, with similarities and differences that can guide us to unveil the various mechanisms that shape atmosphere dynamics at low latitudes in fast-rotating giant planets.

Methods

Image acquisition

Jupiter represents a bright target for JWST. We explored the various filters and strategies in which Jupiter could be observed with NIRCam without saturating the detectors[49]. Image saturation was avoided by exposing the planet in filters centred in strong absorption bands of the Jovian atmosphere (F212N, F335M) and using the shortest integration times possible. In filters where the planet is brighter (F164N, F360M and F405N) we used subarrays (SUB640) that reduce the minimum exposure time. In all cases we used rapid readout patterns. We designed a pointing sequence in which gaps between the four NIRCam B detectors can be recovered with an appropriate dither pattern using four exposures separated in time by only a few minutes. Images obtained using a full array configuration were acquired with a dither pattern of three positions.

Image processing and composition

We used the NIRCam calibration processing pipeline[50] to produce calibrated and geometrically corrected versions of the images with different exposure levels from the original uncalibrated images. NIRCam detectors were read out non-destructively three times for each image, conserving the charge in each pixel and forming different versions of the same image (groups) with different accumulated exposures. We used a combination of one, two and three groups in images obtained in full arrays, and versions of the images from only two and three groups in images obtained using subarrays to remove saturated areas, produce sharp images without rotational smearing, and obtain high signal-to-noise ratio through our images. We used an adaptive median filter to remove bad pixels identified by the pipeline. We navigated each individual image and subframe separately comparing the position of the planet with a synthetic longitude–latitude grid using the WinJupos software due to its flexible use. These navigations were compared with navigation obtained with python code using World Coordinate System information from the telescope pointing, finding good agreement. Images obtained with small time separations of a few minutes were combined with WinJupos correcting the rotation of the planet and producing higher signal-to-noise-ratio images. These were high-pass filtered to enhance the contrast of small-scale faint features in the planet and reduce limb-darkening effects. The images were map-projected, oversampling the initial resolution of the images, that is the resolution used

in the maps was greater than that of the original images, limb-darkened corrected and further enhanced with high-pass filters.

Winds analysis

Maps of the planet were compared using the PICV3 software[51,39]. This software performs one- or two-dimensional correlations over two images using boxes whose size can be configured and adapted to the contrast of the region of the image where the analysis is run. Winds were measured over the final composed images except in the F164N images, where image pairs over the same B detector were compared individually producing 16 individual data sets that were later merged into a single zonal wind profile. PICV3 has a graphical user interface that allows selection of specific regions of the images. We avoided regions with large-scale features and examined the equatorial region with long boxes with typical longitudinal sizes of 20° and latitudinal sizes of 1°. The F164N images were analysed using 16 image pairs from the combination of 4 subarrays and 3 dither positions combining the results from the individual zonal wind profiles in a single zonal wind profile in that filter.

Data availability

Source data for this paper are available at: https://github.com/JWSTGiantPlanets/Jupiter-Atmosphere-NIRCAM. This dataset is associated with the following https://doi.org/10.5281/zenodo.8199030. JWST and HST data used in this paper were obtained from the Mikulski Archive for Space Telescopes at the Space Telescope Science Institute (https://archive.stsci.edu/), which is operated by the Association of Universities for Research in Astronomy, Inc., under NASA contract NAS 5-03127 for the JWST and under NASA contract NAS 5-26555 for the HST. JWST ERS 1373 observations of Jupiter's atmosphere used in this publication are available at https://doi.org/10.17909/vc7n-p631. HST context observations obtained on 28 July 2022 are available at: https://doi.org/10.17909/rnp9-gj41. HST/OPAL maps of Jupiter from 2019 and Saturn from 2022 are available at https://doi.org/10.17909/T9G593. Amateur observations used to provide temporal context to our JWST observations can be downloaded from the PVOL (http://pvol2.ehu.eus) and ALPO Japan (https://alpo-j.sakura.ne.jp/indexE.htm) databases. Source data are provided with this paper.

Code availability

JWST/NIRCAM calibration software is available at https://github.com/spacetelescope/jwst and is documented online at https://jwst-docs.stsci.edu/jwst-science-calibration-pipeline-overview. WinJupos software is available at http://jupos.org/gh/download.htm. The image correlation software used in this study (PICV3) is available at https://doi.org/10.5281/zenodo.4312675.

References

1. Ingersoll, A. P. et al. in *Jupiter: The Planet, Satellites and Magnetosphere* (eds Bagenal, F., Dowling, T. E. & McKinnon, W. B.) Ch. 6 (Cambridge Univ. Press, 2004).
2. Sánchez-Lavega, A. et al. in *Zonal Jets: Phenomenology, Genesis, Physics* (eds Galperin, B. & Read, P. L.) Ch. 4 (Cambridge Univ. Press, 2019).
3. Guillot, T. et al. A suppression of differential rotation in Jupiter's deep interior. *Nature* **555**, 227–230 (2018).
4. Kaspi, Y. et al. Jupiter's atmospheric jet streams extend thousands of kilometres deep. *Nature* **555**, 223–226 (2018).
5. Galanti, E. et al. Saturn's deep atmospheric flows revealed by the Cassini Grand Finale gravity measurements. *Geophys. Res. Lett.* **46**, 616–624 (2019).
6. Iess, L. et al. Measurement and implications of Saturn's gravity field and ring mass. *Science* **364**, aat2965 (2019).
7. García-Melendo, E., Sánchez-Lavega, A., Rojas, J. F., Pérez-Hoyos, S. & Hueso, R. Vertical shears in Saturn's eastward jets at cloud level. *Icarus* **201**, 818–820 (2009).
8. Fletcher, L. N. et al. Mid-infrared mapping of Jupiter's temperatures, aerosol opacity and chemical distribution with IRTF/TEXES. *Icarus* **278**, 128–161 (2016).
9. Barbara, J. M. & Del Genio, A. D. Tropopause and lower stratosphere winds and eddy fluxes on Saturn as seen by Cassini imaging. *Icarus* **354**, 114095 (2020).
10. García-Melendo, E., Sánchez-Lavega, A., Legarreta, J., Pérez-Hoyos, S. & Hueso, R. A strong high altitude narrow jet detected at Saturn's equator. *Geophys. Res. Lett.* **37**, L22204 (2010).
11. Sánchez-Lavega, A. et al. An enduring rapidly moving storm as a guide to Saturn's Equatorial jet's complex structure. *Nat. Commun.* **7**, 13262 (2016).
12. Andrews, D. G., Holton, J. R. & Leovy, C. B. *Middle Atmosphere Dynamics* (Academic, 1987).
13. Marcus, P. S., Tollefson, J., Wong, M. H. & de Pater, I. An equatorial thermal wind equation: applications to Jupiter. *Icarus* **324**, 198–223 (2019).
14. Flasar, F. M. et al. An intense stratospheric jet on Jupiter. *Nature* **427**, 132–135 (2004).
15. Fouchet, T. et al. An equatorial oscillation in Saturn's middle atmosphere. *Nature* **453**, 200–202 (2008).
16. Leovy, C. B., Friedson, A. J. & Orton, G. S. The quasiquadrennial oscillation of Jupiter's equatorial stratosphere. *Nature* **354**, 380–382 (1991).
17. Friedson, A. J. New observations and modelling of a QBO-like oscillation in Jupiter's stratosphere. *Icarus* **137**, 34–55 (1999).
18. Orton, G. S. et al. Semi-annual oscillations in Saturn's low-latitude stratospheric temperatures. *Nature* **453**, 196–199 (2008).
19. Baldwin, M. P. et al. The quasi-biennial oscillation. *Rev. Geophys.* **39**, 179–229 (2001).
20. Giles, R. S., Greathouse, T. K., Cosentino, R. G., Orton, G. S. & Lacy, J. H. Vertically-resolved observations of Jupiter's quasi-quadrennial oscillation from 2012 to 2019. *Icarus* **350**, 113905 (2020).
21. Guerlet, S., Fouchet, T., Bézard, B., Flasar, F. M. & Simon-Miller, A. A. Evolution of the equatorial oscillation in Saturn's stratosphere between 2005 and 2010 from Cassini/CIRS limb data analysis. *Geophys. Res. Lett.* **38**, L09201 (2011).
22. Guerlet, S. et al. Equatorial oscillation and planetary wave activity in Saturn's stratosphere through the Cassini epoch. *J. Geophys. Res. Planets* **123**, 246–261 (2018).
23. Schinder, P. J. et al. Saturn's equatorial oscillation: Evidence of descending thermal structure from Cassini radio occultations. *Geophys. Res. Lett.* **38**, L08205 (2011).
24. Antuñano, A. et al. Fluctuations in Jupiter's equatorial stratospheric oscillation. *Nat. Astron.* **5**, 71–77 (2021).
25. Fletcher, L. N. et al. Disruption of Saturn's quasi-periodic equatorial oscillation by the great northern storm. *Nat. Astron.* **1**, 765–770 (2017).
26. Orton, G. S. et al. Unexpected long-term variability in Jupiter's tropospheric temperatures. *Nat. Astron.* **7**, 190–197 (2023).
27. Banfield, D. et al. Jupiter's cloud structure from Galileo imaging data. *Icarus* **135**, 230–250 (1998).
28. López-Puertas, M. et al. Aerosols and water ice in Jupiter's stratosphere from UV-NIR ground-based observations. *Astron. J.* **156**, 169 (2018).
29. West, R. A. et al. in *Jupiter. The Planet, Satellites and Magnetosphere* (eds Bagenal, F., Dowling, T. E. & McKinnon, W.B.) Ch. 5 (Cambridge Univ. Press, 2004).
30. Fry, P. M. & Sromovsky, L. A. Investigating temporal changes in Jupiter's aerosol structure with rotationally-averaged 2015-2020 HST WFC3 images. *Icarus* **389**, 115224 (2023).
31. Wong, M. H. et al. 2008. A shift in Jupiter's equatorial haze distribution imaged with the Multi-Conjugate Adaptive Optics Demonstrator at the VLT. Preprint at https://doi.org/10.48550/arXiv.0810.3703 (2008).

32. Johnson, P. E. et al. Longitudinal variability in Jupiter's zonal winds derived from multi-wavelength HST observations. *Planet. Space Sci.* **155**, 2–11 (2018).
33. Li, L. et al. Vertical wind shear on Jupiter from Cassini images. *J. Geophys. Res. Planets* **111** https://doi.org/10.1029/2005JE002556 (2006).
34. Horner, S. D. & Rieke, M. J. The near-infrared camera (NIRCam) for the James Webb Space Telescope (JWST). In *Optical, Infrared, and Millimeter Space Telescopes*, Vol. 5487 (ed. Mather, J. C.) 628–634 (SPIEE, 2004).
35. de Pater, I. et al. JWST observations of the Jovian System from commissioning and ERS data. AAS Division of Planetary Science meeting #54, id. 306.07. *Bull. Am. Astron. Soc.* **54**, e-id 2022n8i306p07 (2022).
36. de Pater, I. et al. Keck adaptive optics images of Jupiter's north polar cap and Northern Red Oval. *Icarus* **213**, 559–563 (2011).
37. Sromovsky, L. A. & Fry, P. M. Composition and structure of fresh ammonia clouds on Jupiter based on quantitative analysis of Galileo/NIMS and New Horizons/LEISA spectra. *Icarus* **307**, 347–370 (2018).
38. Hueso, R., Legarreta, J., García-Melendo, E., Sáchez-Lavega, A. & Pérez-Hoyos, S. The Jovian anticyclone BA. II. Circulation and interaction with the zonal jets. *Icarus* **203**, 499–515 (2009).
39. Hueso, R. et al. Jupiter cloud morphology and zonal winds from ground-based observations before and during Juno's first perijove. *Geophys. Res. Lett.* **44**, 4669–4678 (2017).
40. Hueso, R. Particle Image Correlation Velocimetry Software PICV3. *Zenodo* https://doi.org/10.5281/zenodo.4312675 (2020).
41. Porco, C. C. et al. Cassini imaging of Jupiter's atmosphere, satellites, and rings. *Science* **299**, 1541–1547 (2003).
42. García-Melendo, E. et al. Dynamics of Jupiter's equatorial region at cloud top level from Cassini and HST images. *Icarus* **211**, 1242–1257 (2011).
43. Bardet, D., Spiga, A. & Guerlet, S. Joint evolution of equatorial oscillation and interhemispheric circulation in Saturn's stratosphere. *Nat. Astron.* **6**, 804–811 (2022).
44. Lindzen, R. S. & Holton, J. R. A theory of the quasi-biennial oscillation. *J. Atmos. Sci.* **25**, 1095–1107 (1968).
45. Cosentino, R. G. et al. New observations and modeling of Jupiter's Quasi-Quadrennial Oscillation. *J. Geophys. Res. Planets* **122**, 2719–2744 (2017).
46. Cavalié, T. et al. First direct measurement of auroral and equatorial jets in the stratosphere of Jupiter. *Astron. Astrophys.* **647**, L8 (2021).
47. Benmahi, B. et al. Mapping the zonal winds of Jupiter's stratospheric equatorial oscillation. *Astron. Astrophys.* **652**, A125 (2021).
48. Wong, M. H. et al. High-resolution UV/optical/IR imaging of Jupiter in 2016-2019. *Astrophys. J. Suppl. Ser.* **247**, 25 (2020).
49. Norwood, J. et al. Giant planet observations with the James Webb Space Telescope. *Publ. Astron. Soc. Pac.* **128**, 018005 (2016).
50. Bushouse, H. et al. JWST Calibration Pipeline (1.8.2). *Zenodo* https://doi.org/10.5281/zenodo.7229890 (2022).
51. Tokunaga, A. T. & Vacca, W. D. The Mauna Kea Observatories near-Iinfrared filter set. III. Isophotal wavelengths and absolute calibration. *Publ. Astron. Soc. Pac.* **117**, 421 (2005).

Acknowledgements

This work is based on observations made with the NASA/ESA/CSA JWST. These observations are associated with programme no. 1373, which is led by co-PIs Imke de Pater and Thierry Fouchet. We also used observations made with the NASA/ESA Hubble Space Telescope under programme no. 16913, which provided support to M.H.W. and G.S.O. Jupiter wind data from 2019 and Saturn maps from 2022 in Fig. 5 come from observations acquired from the NASA/ESA Hubble Space Telescope, associated with OPAL programmes GO15502 and GO16790 (PI: A. Simon), which provided support to A.A.S., M.H.W. and G.S.O. R.H., A.S.L. and A.A. were supported by grant PID2019-109467GB-I00 funded by MCIN/AEI/10.13039/501100011033/ and were also supported by Grupos Gobierno Vasco IT1742-22. I.d.P and M.H.W. are in part supported by the Space Telescope Science Institute grant JWST-ERS-01373. L.N.F. and J.H. were supported by a European Research Council Consolidator Grant (under the European Union's Horizon 2020 research and innovation programme, grant agreement no. 723890) at the University of Leicester. J.H. was also supported by an STFC PhD Studentship. Some of this research was carried out at the Jet Propulsion Laboratory, California Institute of Technology, under a contract with the National Aeronautics and Space Administration (80NM0018D0004). K.M.S. was supported in part by NASA grants 80NSSC21K1418 and 80NSSC19K0894. We are grateful to the ensemble of amateur astronomers that observed Jupiter from June through July 2022 and whose observations provided a temporal context to our JWST images of Jupiter. We are also very grateful to G. Hahn for his many years of dedication in creating the WinJupos software whose flexible use greatly simplified the combination of images obtained on different times.

Author contributions

R.H. led the analysis of the NIRCAM images. R.H., A.S.-L. and A.A. made the wind analysis and wrote the first draft of the paper. I.d.P. and T.F. led the JWST ERS team and contributed to the initial interpretation of the data. P.R.-O. led the desaturation of the data using the JWST calibration pipeline. L.A.S. and P.M.F. provided the calculation of filter penetration depths. R.H., I.d.P., T.F., M.H.W., L.N.F., P.M.F., G.S.O., L.A.S., A.S.-L., P.G.J.I., E.L., K.d.K., H.M, S.L.-C. and V.H. contributed to obtaining the data used in this study. All authors discussed the results and commented on the manuscript.

Competing interests

The authors declare no competing interests.

Additional information

Supplementary information The online version contains supplementary material available at https://doi.org/10.1038/s41550-023-02099-2.

Correspondence and requests for materials should be addressed to Ricardo Hueso.

Peer review information *Nature Astronomy* thanks Shawn Brueshaber, Thomas Greathouse and the other, anonymous, reviewer(s) for their contribution to the peer review of this work.